(Received 5 May 2026, Accepted 25 May 2026, Scheduled 9 June 2026)

Design and Optimization of a Flux Reversal Machine with Double-Layer Dual-PM Halbach Array

Jiahao Zhang, Bingnan Feng, Runqing Su, and Libing Jing*

College of Electrical Engineering and New Energy, Hubei Provincial Engineering Technology Research Center for Microgrid China Three Gorges University, Yichang 443002, China

ABSTRACT: The flux reversal machine (FRM) has the advantages of a high utilization rate of permanent magnets (PMs) and a wide speed range. However, it still suffers from low output torque and large torque ripple. In this study, an FRM with a double-layer dual-PM Halbach array (DLDPMH-FRM) is proposed. The PMs are arranged in a double layer at the stator slot, and a Halbach array is employed at the rotor slot opening. The stator and rotor PMs together form a dual-PM structure. The response surface method (RSM) and multi-objective genetic algorithm (MOGA) were combined for global optimization. Compared with the dual-PM FRM (DPM-FRM), the torque of the DLDPMH-FRM reaches 7.75 N·m, which is 35.72% higher than that of the DPM-FRM, whereas the torque ripple is reduced by 86.01%. This model provides a feasible solution for the design and optimization of high-performance FRM.

1. INTRODUCTION

In response to the increasingly severe energy shortage, high-power-density machines have become an important research direction in the field of electrical engineering [1]. However, in application scenarios requiring high dynamic performance and high reliability, conventional permanent magnet (PM) machines gradually exhibit problems, such as low torque density and large torque ripple [2]. Therefore, it is of great significance to study new high-torque-density machines [3].

As a typical magnetic field modulation machine, the flux reverse machine (FRM) has the advantages of a high utilization rate of PMs, simple structure, and suitability for high-speed operation [4]. Recently, it has received extensive attention [5]. Simultaneously, FRM shows good application prospects in the fields of new-energy vehicle drive and distributed generation [6]. However, there are still some problems, such as limited output torque and large torque ripple, which need to be further addressed [7–9].

Currently, researchers focus on these two core issues and optimize them along three main technical lines. The first is a dual-PM structure. In [10], the flux regulation and torque capability of the FRM and dual-PM FRM (DPM-FRM) were compared, and it was found that the dual-PM machine was better suited for high-torque operation. In [11], the authors placed radially magnetized PM in the rotor slots while retaining the Halbach array in the stator slots, thereby forming a dual-PM structure that effectively improved the utilization of PM materials. In [12], a dual-Halbach array was proposed to solve the flux leakage problem of a dual-winding dual-PM machine. In [13], a dual-stator FRM was proposed. A Halbach array was used at the slot openings of the inner and outer stators. Through prototype verification, it was found to have better torque performance and PM utilization.

The second is the Halbach array. In [14], a consequent-pole FRM with Halbach array magnets embedded at the top of the rotor slots was proposed. By guiding the flux into the rotor teeth, the flux leakage is effectively reduced, improving the PM utilization and torque density. In [15], an alternating "PM-iron" structure was used on both the stator and rotor, and the torque density was improved by utilizing the bidirectional flux modulation effect. In [16], the addition of silicon steel material between the two PMs of a conventional two-stage Halbach array was proposed, which effectively improved the electromagnetic performance of the machine.

The third is a double-layered PM structure. In [17], the authors proposed a coaxial magnetic gear with a dual-layer PM and spoke structure for a tidal power generation scenario. The outer rotor PM is divided into two layers (one layer is a Halbach array, and the other is radial magnetization). Through verification, it was found that the output torque of the proposed structure was increased by 33.42%. In [18], three new dual-layer PM arrangements were proposed. Compared with the conventional single-layer parallel magnetization method, the working harmonic amplitudes of the three new machines were improved, and their electromagnetic performance was improved.

Previous studies have verified the improvement in machine performance by a dual-PM structure, Halbach array, and double PM arrangement. Therefore, an FRM with a double-layer dual-PM Halbach array is proposed in this study. It reduces flux leakage and optimizes the air-gap magnetic field, thereby enhancing the torque and back electromotive force (EMF). Simultaneously, it reduces cogging torque, suppresses torque ripple, and considers the stability, fault tolerance, and reliability of the operation. The remainder of this paper is organized as

* Corresponding author: Libing Jing (jinglibing163@163.com).

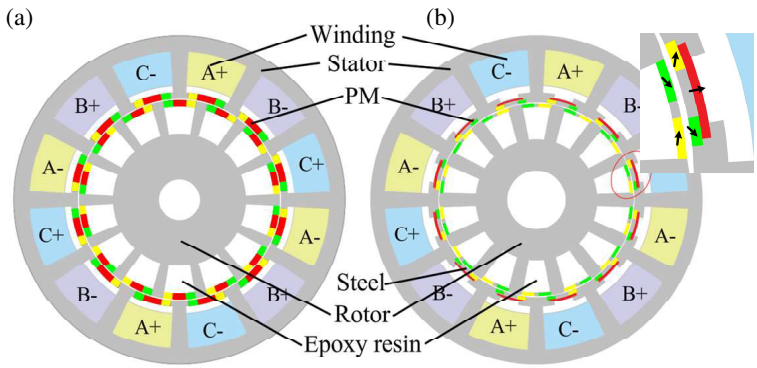

FIGURE 1. The topology of machines (a) Conventional and (b) Proposed.

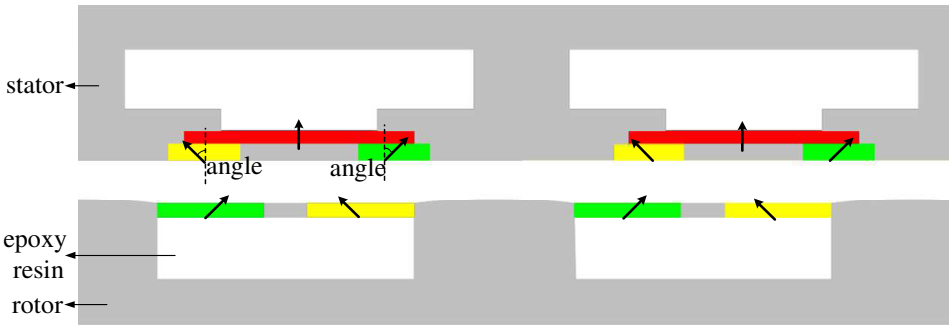

FIGURE 2. PM array expansion diagram.

follows. The topology and working principle of the proposed sensor are introduced in Section 2. In Section 3, the method of combining response surface method (RSM) and multi-objective genetic algorithm (MOGA) is used for global optimization. In Section 4, the performance of the machine is compared based on finite element analysis (FEA). The key contributions of this study are summarized in Section 5.

2. TOPOLOGY AND WORKING PRINCIPLE

2.1. Topology

Figure 1 shows the structural topologies of the two machines. Fig. 1(a) shows the topology of the DPM-FRM. Both the stator and rotor PMs are magnetized by the Halbach array to form a dual-PM structure.

Figure 1(b) shows the topology of the DLDPMH-FRM. The PMs of the DLDPMH-FRM are arranged in double layers at the stator slot. The upper PM is magnetized along the radial direction, and the lower PM is divided into two parts. The auxiliary PMs on both sides are magnetized at a certain angle, and silicon steel is used in the middle to form a new Halbach array of 'PM + silicon steel + PM'. Moreover, a Halbach array was employed at the rotor slot openings. The stator and rotor PMs together form a dual-PM structure. To weaken the adverse effect of non-working harmonics on performance, the rotors of the machine are designed as convex pole teeth with equal inner and outer pole arcs, and the pole shoe is treated eccentrically.

2.2. Working Principle

The DLDPMH-FRM still follows the magnetic field modulation effect in the working principle. Fig. 2 shows the PM array expansion diagram of the DLDPMH-FRM. The stator and rotor PMs use a Halbach array and form a dual-PM structure, which significantly changes the distribution of the magnetomotive force source and air-gap permeability characteristics and improves the electromagnetic performance.

According to the theory of magnetic field modulation, the magnetomotive forces generated by the stator and rotor PMs can be expressed as

$$\begin{cases} F_s(\theta) = \sum\limits_{j=1,3,5,\ldots}^{\infty} F_{S\_\mathrm{PM}} \cos\left(jP_{S\_\mathrm{PM}}\theta\right), \\ F_r(\theta,t) = \sum\limits_{k=1,2,3,\ldots}^{\infty} F_{R\_\mathrm{PM}} \cos\left(kP_{R\_\mathrm{PM}}\left(\theta-\omega_r t\right)\right). \end{cases} \tag{1}$$

where $F_{\mathrm{S\_PM}}$ and $F_{\mathrm{R\_PM}}$ are the Fourier coefficients of the PM magnetomotive force of the stator and rotor, respectively; $p_{\mathrm{S\_PM}}$ and $p_{\mathrm{R\_PM}}$ are the polar pairs of the PM of the stator and rotor, respectively; and ω_r is the mechanical angular velocity of the rotor.

Because of the cogging structure on the surface of the stator and rotor, the air gap permeance changes periodically. The stator-side air-gap permeance can be expressed as

$$\Lambda_s(\theta) = \sum_{a=0,1,2,\ldots}^{\infty} \Lambda_{sv} \cos\left(aN_s\theta\right) \tag{2}$$

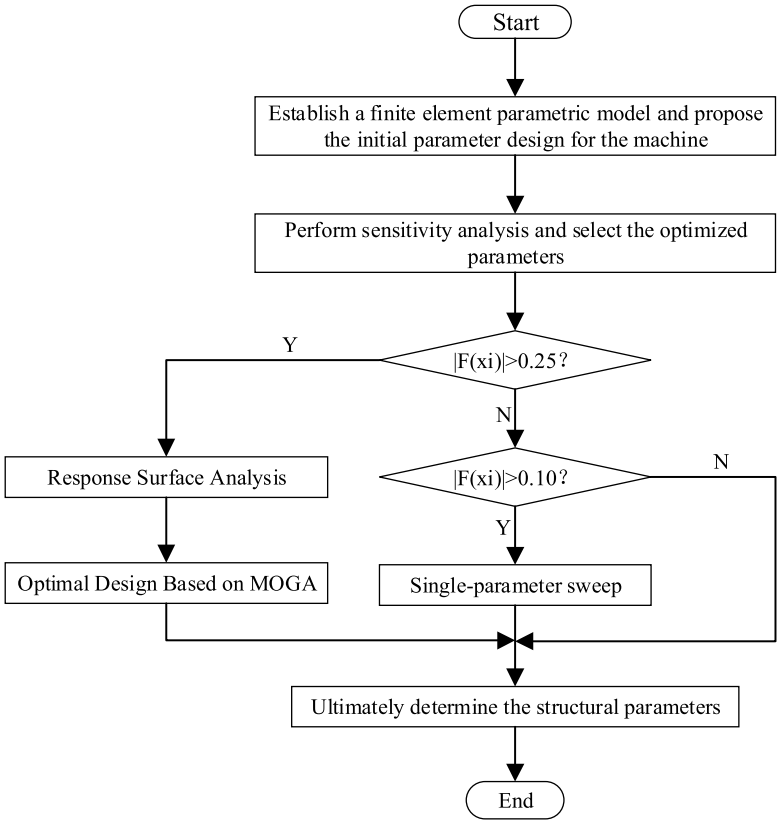

FIGURE 3. Optimization process of the DLDPMH-FRM.

The air gap permeance on the rotor side changes with the rotor position, and the expression is

$$\Lambda_r(\theta,t)=\sum_{b=0,1,2,\ldots}^{\infty}\Lambda_{rw}\cos\left(bN_r\left(\theta-\omega_r t\right)\right) \tag{3}$$

where N_s and N_r are the number of stator and rotor teeth, respectively, and Λ_{sv} and Λ_{rw} are the corresponding Fourier coefficients.

Under the excitation of a double-layer PM, the air-gap flux density is modulated by the magnetomotive force of the stator and rotor and the air gap permeance.

$$B_{g,r}(\theta,t)=F_r(\theta,t)\cdot\Lambda_s(\theta) \tag{4}$$

$$=\sum_{k=1,2,3,\ldots}^{\infty}\sum_{a=0,1,2,\ldots}^{\infty}\frac{F_{R\_\mathrm{PM}}\Lambda_{sv}}{2}$$

$$\cos\left(\left(kP_{R\_\mathrm{PM}}\pm aN_s\right)\theta-kP_{R\_\mathrm{PM}}\omega_r t\right) \tag{5}$$

As can be seen from Equations (4) and (5), the pole-pair numbers of the air-gap magnetic flux density harmonics generated by the modulated stator and rotor PM fields can be uniformly expressed as

$$\begin{cases}P_{k,s}=\left|bN_r\pm jP_{\mathrm{PM}\_s}\right|,\\ P_{k,r}=\left|kP_{\mathrm{R\_PM}}\pm aN_s\right|.\end{cases} \tag{6}$$

where $b=0,1,2,\ldots$; $j=1,3,5,\ldots$; $k=1,2,3,\ldots$; $a=0,1,2,\ldots$.

For the machines in this study, $N_s=12$, $N_r=14$. The DPM-FRM and DLDPMH-FRM adopt the dual-PM structure and Halbach array. The number of PM poles of the stator satisfies $p_{\mathrm{S\_PM}}=N_s=12$, and the number of PM poles of the rotor satisfies $p_{\mathrm{R\_PM}}=N_r=14$. By using the above formula, the main working harmonic orders of the two machines are the same, which are 2, 12, 14, and 26 times. However, the DLDPMH-FRM increases the magnetomotive force Fourier coefficients $F_{\mathrm{S\_PM}}$ and $F_{\mathrm{R\_PM}}$, and improves the air gap permeance distribution, so that the working harmonic amplitude of the same order is higher than that of the conventional machine. The subsequent FEA also fully verifies this result.

3. PARAMETER OPTIMIZATION

To ensure that the DPM-FRM and DLDPMH-FRM were compared under the same conditions, the same values were used for the selection of the basic materials and parameters, as shown in Table 1.

The structural parameters of the FRM are numerous and coupled. It is difficult to obtain the global optimal solution using conventional single-parameter scanning. In this study, the optimization strategy combining RSM and MOGA was adopted. The surrogate model was constructed by RSM to accurately capture the nonlinear relationship between parameters and response, and then MOGA was used for efficient global optimization, which greatly improves optimization efficiency. The specific process is shown in Fig. 3.

TABLE 1. Basic parameters.

Parameters	Value
Material of PM	NdFeB
Material of Iron	DW310-35
Axial length/(mm)	60
Stator outer radius/(mm)	120
Length of air gap/(mm)	0.7
Speed/(r/min)	600
Series turns per phase	30
Rated current/(A)	10

3.1. Sensitivity Analysis

In the practical application of FRM, torque and torque ripple are two key indicators for measuring the machine performance. However, there are often constraints between these two optimization objectives. To achieve a balance between the two, this study established the following multi-objective optimization function:

$$F(x_i) = \lambda_1 |G_{0i}(x_i)| + \lambda_2 |G_{\text{kri}}(x_i)|. \quad (7)$$

where $|G_{0i}(x_i)|$ and $|G_{\text{kri}}(x_i)|$ are the torque and torque ripple under the design variables, respectively, and λ_1 and λ_2 are the weight coefficients. The model is mainly designed to reduce the ripple of the FRM, and the torque output capacity needs to be maintained at a reasonable level. Therefore, this study considers the values of $\lambda_1 = 0.4$ and $\lambda_2 = 0.6$.

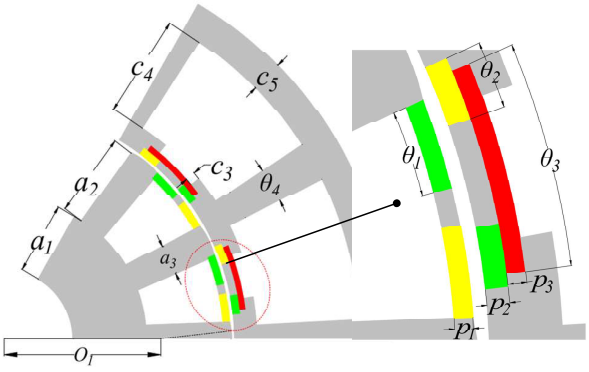

FIGURE 4. Structural parameters.

Figure 4 shows the parameter settings of the proposed machines. Fig. 5 shows the sensitivity of each parameter to the torque and torque ripple of the DLDPMH-FRM. Among them, c_4 and a_3 have the greatest influence on the torque, indicating that the electromagnetic force density is highly sensitive to these parameters. a_3 is the most sensitive to changes in torque ripple and has an obvious control effect on torque ripple. The effects of a_2 and c_5 on the two were relatively small.

Using Equation (7), the influence degree of each parameter on the optimization target was calculated and sorted. According to the analysis results, $|F(x_i)|$ higher than 0.24 is defined as high sensitivity, that between 0.10 and 0.24 defined as medium sensitivity, and that less than 0.10 defined as low sensitivity. The specific results are shown in Table 2. For high sensitivity parameters, RSM and MOGA are combined to optimize.

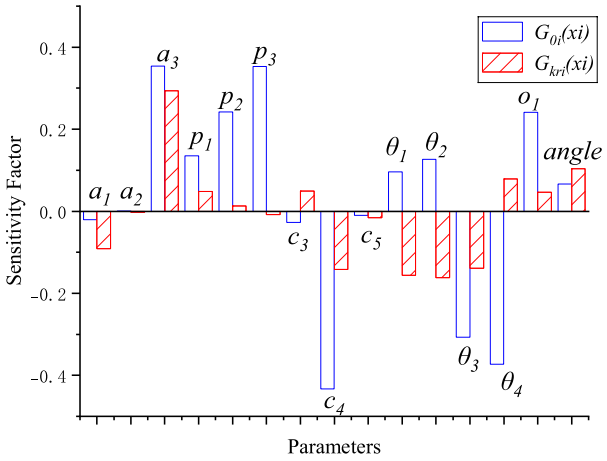

FIGURE 5. Parameter sensitivity analysis.

TABLE 2. Sensitivity analysis and parameter ranges.

Stratification	Parameters	$F(x_i)$	Initial	Scope
Strong sensitivity	a_3 (mm)	0.3238	2.7	2.0–3.0
	c_4 (mm)	0.2875	16.0	14.0–18.0
	o_1 (mm)	0.2516	24.5	24.0–25.0
Medium sensitivity	θ_2 (deg)	0.2259	5.1	4.2–5.6
	θ_3 (deg)	0.2230	5.2	5.0–6.8
	p_3 (mm)	0.1803	0.8	0.6–1.2
	angle (deg)	0.1537	63.4	60.0–75.0
	p_2 (mm)	0.1276	1.0	0.8–1.2
	θ_1 (deg)	0.1258	3.7	3.1–4.2
	p_1 (mm)	0.0915	0.9	0.6–1.1
	θ_4 (deg)	0.0846	9.5	9.0–10.5
Weak sensitivity	c_3 (mm)	0.0381	1.5	–
	a_1 (mm)	0.0298	11.2	–
	c_5 (mm)	0.0128	4.9	–
	a_2 (mm)	0.0012	13.0	–

The medium sensitivity parameters are optimized by single-parameter scanning. The low sensitivity parameters have little influence on the motor and are not optimized.

3.2. RSM and MOGA

For the three parameters selected above, we used the method of combining RSM and MOGA for optimization. The RSM results corresponding to these three parameters are shown in Figs. 6, 7, and 8, respectively.

Figure 6 shows that with an increase in c_4, the torque gradually decreases, and the torque ripple first decreases and then increases. The increase in o_1 will change the effect of c_4: with the increase in o_1, the weakening effect of c_4 on torque is weakened, and the torque decreases slowly. The influence of c_4 on torque ripple changes from a decrease to an increase and then to a continuous increase. This indicates that the interaction between o_1 and c_4 on the torque ripple is significant.

The data in Fig. 7 show that as a_3 increases, the torque gradually increases, and the torque ripple increases. With an in-

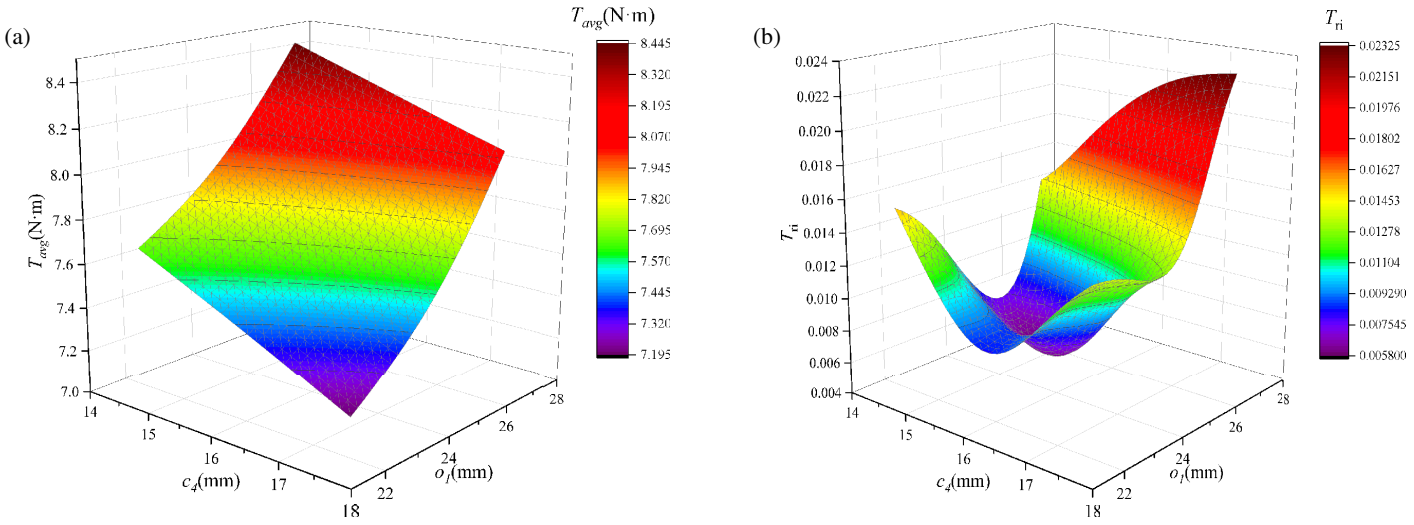

FIGURE 6. Changes of torque characteristics with c_4 and o_1. (a) Average torque. (b) Torque ripple.

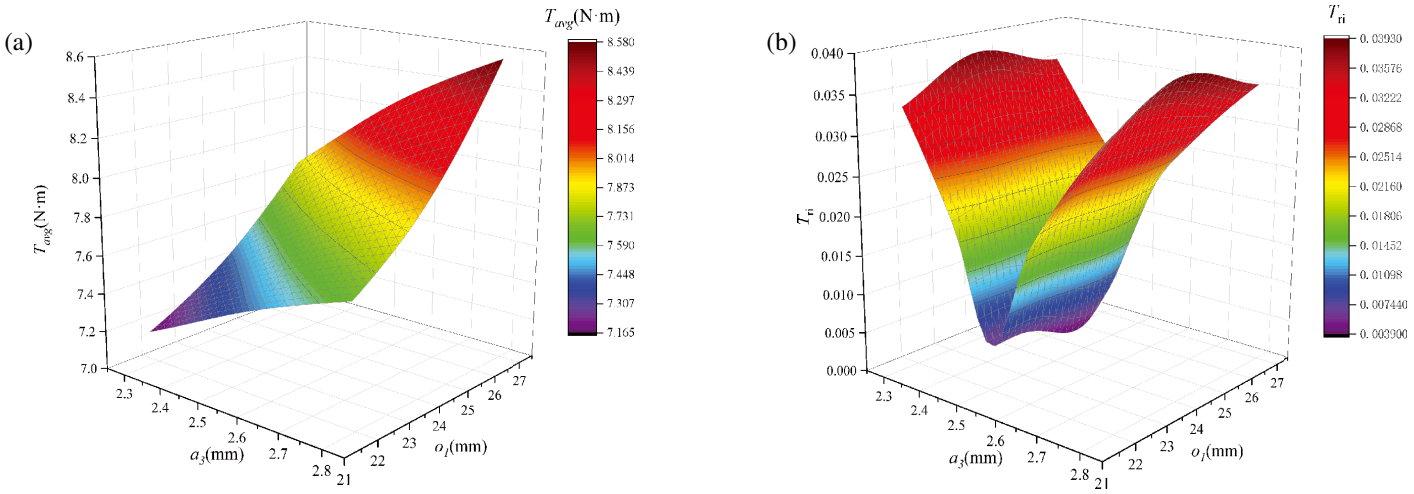

FIGURE 7. Changes of torque characteristics with a_3 and o_1. (a) Average torque. (b) Torque ripple.

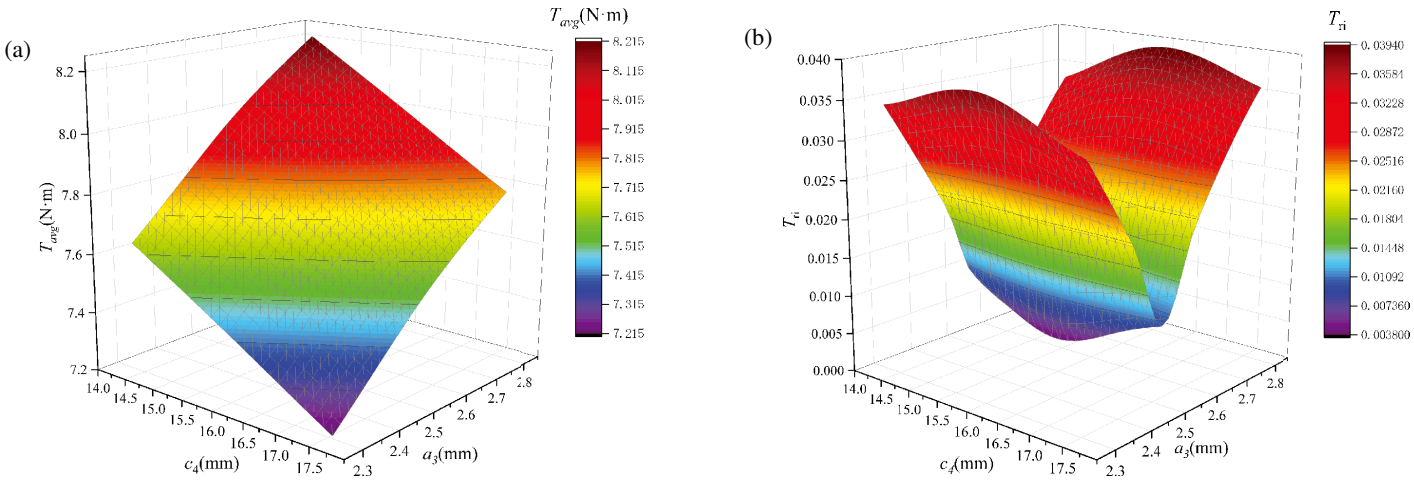

FIGURE 8. Changes of torque characteristics with c_4 and a_3. (a) Average torque. (b) Torque ripple.

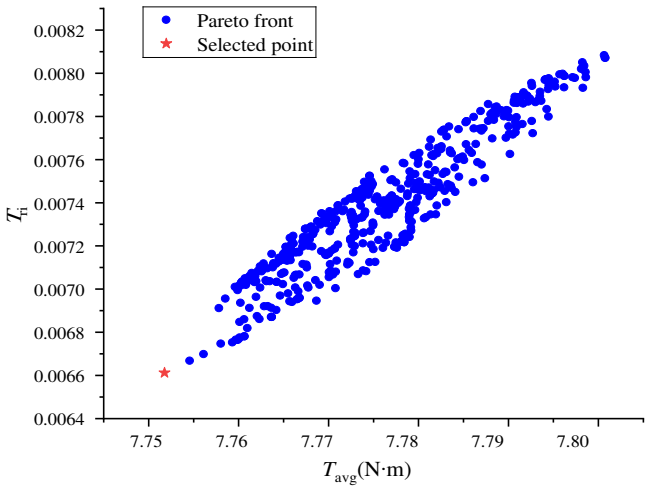

FIGURE 9. Optimization result.

crease in o_1, the change trend of torque and torque ripple does not change significantly, indicating that the interaction between o_1 and a_3 on machine performance is weak.

From the data in Fig. 8, it can be seen that with an increase in c_4, the torque gradually decreases, and the torque ripple remains constant. It is worth noting that with an increase in a_3, the downward trend of torque continues to slow down, and the torque ripple first decreases and then increases, indicating that the interaction between c_4 and a_3 on the machine torque ripple is strong.

Figure 9 shows the distribution of the candidate points of the DLDPMH-FRM. As the torque increased, the torque ripple also increased. Because the goal of this model is to reduce the torque ripple, the torque ripple is selected as the key target, and the candidate points meet this requirement.

3.3. Optimization of Weakly Sensitive Parameters

For the medium-sensitive parameters identified in the sensitivity analysis, the single-parameter scanning method was used for optimization. Fig. 10(a) shows the influence of θ_3 on the torque and ripple. With an increase in θ_3, the torque first increases and then decreases, and the ripple first decreases and then oscillates. When $\theta_3 = 6.2°$, the torque ripple reached the minimum value, and the torque also tended to be near the maximum value, which satisfied the optimization goal. The analysis principle of Fig. 10(b) is similar, and the torque ripple reaches a minimum at $\theta_2 = 4.8°$. After the above parameter optimization, all the parameters of the conventional and proposed machines are summarized in Table 3.

4. ELECTROMAGNETIC PERFORMANCE

To further verify the reliability and effectiveness of the optimization method of RSM and MOGA, two-dimensional finite element models of the optimized DPM-FRM and DLDPMH-FRM were established. Through simulation and modeling, the electromagnetic properties, such as back-EMF and torque, between the two models were compared.

TABLE 3. Summary of all parameter optimization results.

Parameters	DPM-FRM	DLDPMH-FRM
a_1 (mm)	16.39	11.20
a_2 (mm)	12.27	13.00
a_3 (mm)	–	2.47
p_1 (mm)	2.03	0.88
p_2 (mm)	2.19	1.08
p_3 (mm)	–	0.90
c_3 (mm)	–	1.50
c_4 (mm)	15.29	16.00
c_5 (mm)	5.58	4.90
θ_1 (deg)	2.82	3.60
θ_2 (deg)	–	4.80
θ_3 (deg)	4.94	6.20
θ_4 (deg)	3.33	9.70
o_1 (mm)	–	24.25
angle (deg)	–	65.40

4.1. Air Gap Flux Density

Figure 11 shows the radial air gap flux density of the DPM-FRM with the DLDPMH-FRM. From the diagram, it can be seen that the peak magnetic density of the DLDPMH-FRM increases significantly, and the spatial waveform is more abundant, which is also verified by the fast Fourier transform (FFT) spectrum quantification. The richer operating harmonics provide an additional contribution to the electromagnetic torque, which essentially explains the DPFRM torque enhancement.

4.2. No-Load Back EMF

Figure 12 shows the no-load back-EMF waveform and harmonic spectrum of the two machines. It can be clearly seen from the diagram that the back-EMF amplitude of the DLDPMH-FRM is higher than that of the DPM-FRM. Under the same conditions, the peak value of back EMF was 23.5 V, which was 42.25% higher than that of the DPM-FRM (16.52 V). This improvement is attributed to two aspects: the use of a double-layer dual-PM structure and the use of a Halbach array.

However, it can be seen from the diagram that the waveform distortion of DLDPMH-FRM is higher than that of DPM-FRM, and we use THD to calculate the degree of distortion. The smaller the THD is, the better the sine degree of the waveform is. Through calculation, the THD = 1.78% of the DPM-FRM and THD = 3.05% of DLDPMH-FRM are obtained. Although the distortion rate of the DLDPMH-FRM was higher than that of the DPM-FRM, it was less than 5%, which met the design requirements.

4.3. Cogging Torque

Figure 13 shows the cogging torque of the two machines. The peak cogging torque of the DPM-FRM was 95.17 mN·m, whereas that of the DLDPMH-FRM was 37.92 mN·m. The comparison waveform shows that the peak-to-peak value of the

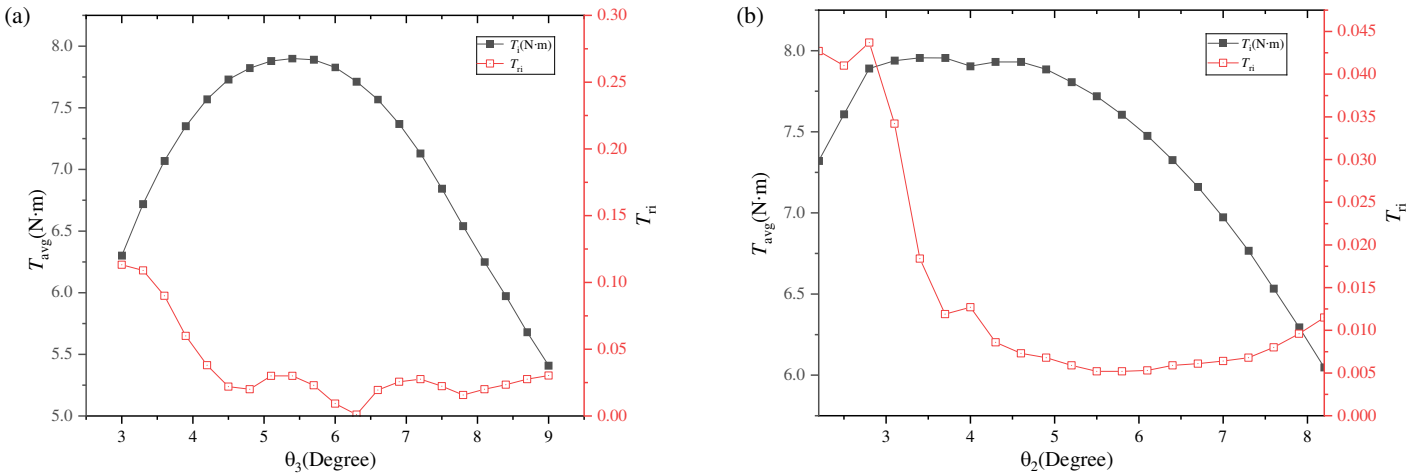

FIGURE 10. Single parameter scanning. (a) Torque characteristics change with θ_3. (b) Torque characteristics change with θ_2.

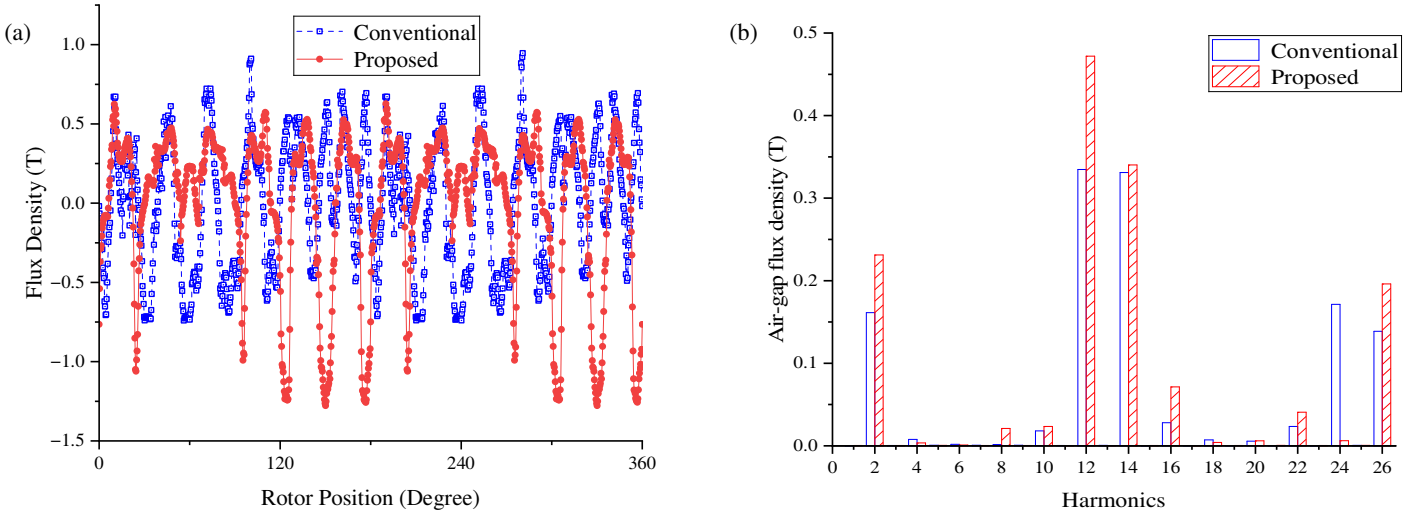

FIGURE 11. Radial air-gap flux density of DPM-FRM and DLDPMH-FRM. (a) Waveform. (b) Harmonic spectra.

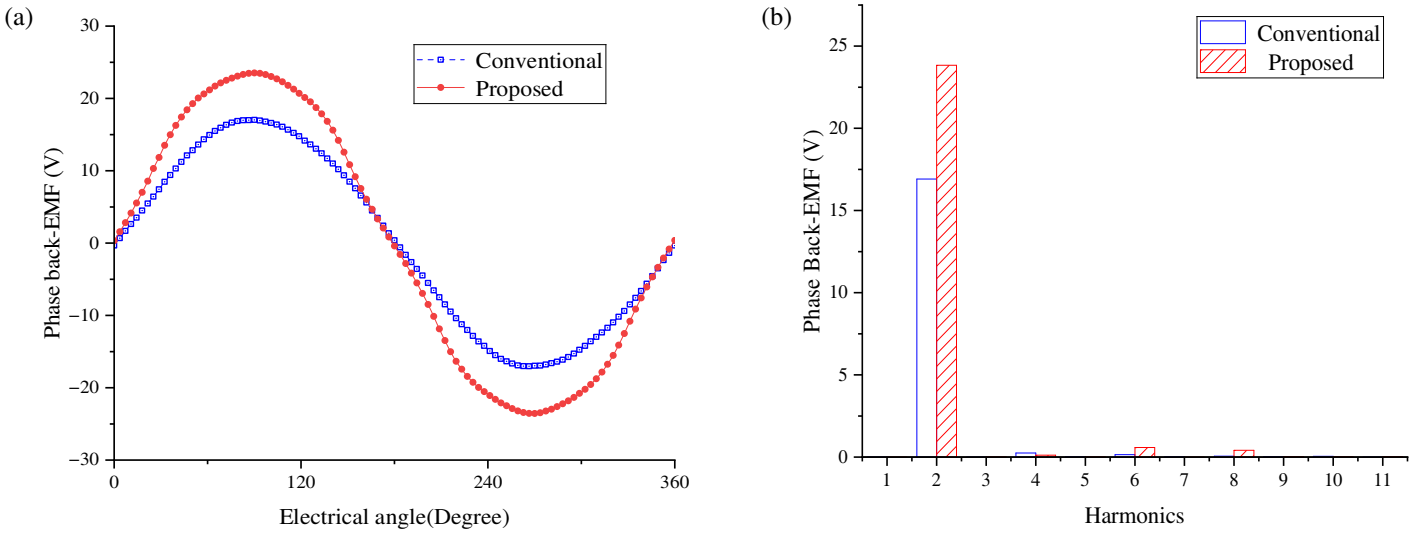

FIGURE 12. Back EMF. (a) Waveform, (b) Harmonic spectrum.

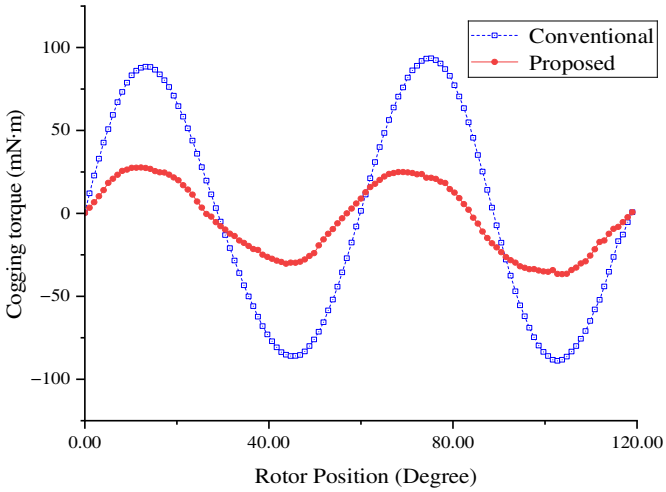

FIGURE 13. Cogging torque of DPM-FRM and DLDPMH-FRM.

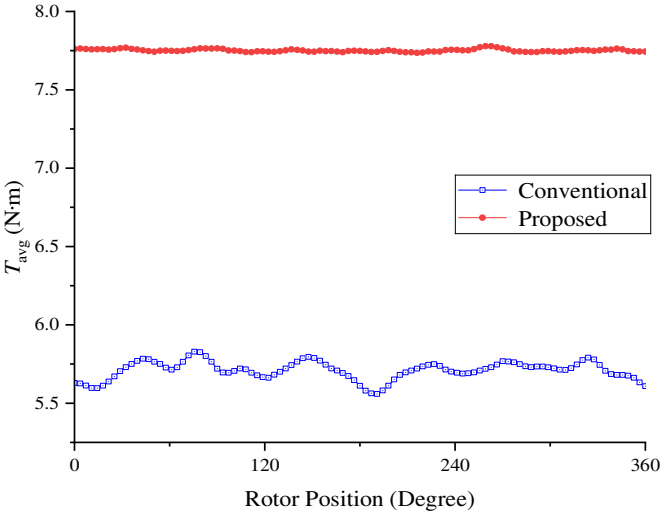

FIGURE 14. Torque.

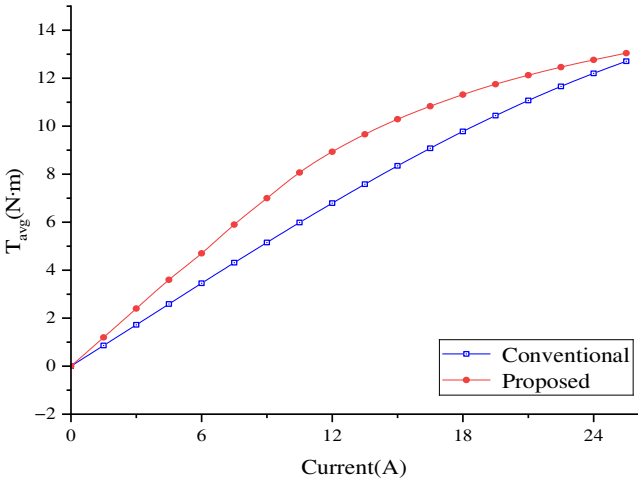

FIGURE 15. Overload capacity of DPM-FRM and DLDPMH-FRM.

cogging torque of the proposed machine is significantly lower than that of the conventional structure, which fundamentally weakens the low-speed torque ripple of the machine and is conducive to reducing the mechanical vibration and electromagnetic noise during the operation of the entire machine.

4.4. Torque

While the cogging torque is improved, the load performance of the machine also shows significant advantages, which directly reflect the torque and torque ripple of the machine. Fig. 14 shows the electromagnetic torque of the two machines under rated current excitation. The average torque of the DLDPMH-FRM reached 7.75 N·m, which was 35.72% higher than that of the DPM-FRM (5.71 N·m). In terms of torque ripple, the DPM-FRM was 4.72%, and the DLDPMH-FRM was reduced to 0.66%, a decrease of 86.01%. The amount of PM was significantly reduced.

4.5. Overload Capacity

Figure 15 shows the overload capacity curves of the two machines. It can be observed that the DLDPMH-FRM provides a higher torque at the rated current and exhibits better working ability under rated conditions. However, with an increase in current, the torque growth rate decreases owing to the stronger magnetic saturation effect; however, the unit PM still exhibits a higher torque output efficiency.

5. CONCLUSION

In this study, an FRM with a double-layer dual-PM Halbach array is discussed, and the global optimization of the machine is performed using the RSM and MOGA. Through FEA and verification, several conclusions were drawn.

1) Under no-load conditions, the harmonic content of air gap flux density of DLDPMH-FRM is higher than that of the DPM-FRM, resulting in a relatively large distortion of the no-load back-EMF waveform. Its no-load back-EMF amplitude reaches 23.5 V, which is 42.25% higher than that of the conventional machine. The cogging torque is reduced from 95.17 mN·m of the traditional motor to 37.92 mN·m.

2) Under the rated current, the torque of DLDPMH-FRM reaches 7.75 N·m, which is 35.72% higher than that of DPM-FRM. The torque ripple is reduced from 4.72% to 0.66%. Under overload conditions, the machine also exhibits good torque output characteristics.

Nevertheless, the back-EMF waveform distortion will introduce additional harmonic iron loss and electromagnetic vibration noise. In the follow-up study, further attention should be paid to the optimization design of harmonic suppression.

ACKNOWLEDGEMENT

This work was supported by the National Natural Science Foundation of China (Grant No. 52477056).

REFERENCES

[1] Pellegrino, G., A. Vagati, P. Guglielmi, and B. Boazzo, "Performance comparison between surface-mounted and interior PM motor drives for electric vehicle application," *IEEE Transactions on Industrial Electronics*, Vol. 59, No. 2, 803–811, Feb. 2012.

[2] Gao, Y., D. Li, R. Qu, and Z. Liang, "Analysis of novel flux reversal permanent-magnet machine with multi MMF working harmonics," in *2018 IEEE Energy Conversion Congress and Exposition (ECCE)*, 6484–6491, Portland, OR, USA, 2018.

[3] Cheng, M., W. Hua, J. Zhang, and W. Zhao, "Overview of stator-permanent magnet brushless machines," *IEEE Transactions on Industrial Electronics*, Vol. 58, No. 11, 5087–5101, Nov. 2011.

[4] Yang, H., Z. Q. Zhu, H. Lin, H. Li, and S. Lyu, "Analysis of consequent-pole flux reversal permanent magnet machine with biased flux modulation theory," *IEEE Transactions on Industrial Electronics*, Vol. 67, No. 3, 2107–2121, Mar. 2020.

[5] Li, H. Y. and Z. Q. Zhu, "Analysis of flux-reversal permanent-magnet machines with different consequent-pole PM topologies," *IEEE Transactions on Magnetics*, Vol. 54, No. 11, 1–5, 2018.

[6] Chen, H., A. M. El-Refaie, and N. A. O. Demerdash, "Flux-switching permanent magnet machines: A review of opportunities and challenges — Part I: Fundamentals and topologies," *IEEE Transactions on Energy Conversion*, Vol. 35, No. 2, 684–698, Jun. 2020.

[7] Wu, L., Y. Zheng, Y. Fang, and X. Huang, "Novel fault-tolerant doubly fed flux reversal machine with armature windings wound on both stator and rotor teeth," *IEEE Transactions on Industrial Electronics*, Vol. 68, No. 6, 4780–4789, 2021.

[8] Qi, J., Z. Q. Zhu, L. Yan, G. W. Jewell, C. Gan, Y. Ren, S. Brockway, and C. Hilton, "Suppression of torque ripple for consequent pole PM machine by asymmetric pole shaping method," *IEEE Transactions on Industry Applications*, Vol. 58, No. 3, 3545–3557, 2022.

[9] Mohammadi, A., O. A. Badewa, Y. Chulaee, and D. M. Ionel, "Two-level design optimization of AC machines with DC stator excitation and minimal torque ripple using reluctance rotor profile shaping," in *2024 IEEE Energy Conversion Congress and Exposition (ECCE)*, 5174–5179, Phoenix, AZ, USA, 2024.

[10] Wei, F., Z. Q. Zhu, Y. Zheng, and H. Xu, "Comparative study of stator-PM and dual-PM consequent-pole hybrid excited flux-reversal machines," in *2022 25th International Conference on Electrical Machines and Systems (ICEMS)*, 1–5, Chiang Mai, Thailand, 2022.

[11] Aslani, B., S. E. Abdollahi, and S. A. Gholamian, "A novel dual-PM flux reversal machine with Halbach array magnets in stator slots," in *2023 3rd International Conference on Electrical Machines and Drives (ICEMD)*, 1–5, Tehran, Iran, 2023.

[12] Sun, P., S. Jia, D. Yang, D. Liang, and Z. Luo, "Design and comparative analysis of dual winding dual magnet machines with different PM arrangements," *IEEE Transactions on Industry Applications*, Vol. 61, No. 1, 151–160, Jan.–Feb. 2025.

[13] Zheng, Y., L. Wu, J. Zhu, Y. Fang, and L. Qiu, "Analysis of dual-armature flux reversal permanent magnet machines with halbach array magnets," *IEEE Transactions on Energy Conversion*, Vol. 36, No. 4, 3044–3052, Dec. 2021.

[14] Yang, K., F. Zhao, Y. Wang, and Z. Bao, "Consequent-pole flux reversal permanent magnet machine with halbach array magnets in rotor slot," *IEEE Transactions on Magnetics*, Vol. 57, No. 2, 1–5, 2021.

[15] Wang, Q., S. Niu, and L. Yang, "Design optimization and comparative study of novel dual-PM excited machines," *IEEE Transactions on Industrial Electronics*, Vol. 64, No. 12, 9924–9933, Dec. 2017.

[16] Ni, Y., L. Zhang, and Z. Qiu, "Comparison of FRPM machines with different magnet arrangements," in *2023 IEEE 6th International Electrical and Energy Conference (CIEEC)*, 112–115, Hefei, China, 2023.

[17] Jing, L., W. Liu, W. Tang, and R. Qu, "Design and optimization of coaxial magnetic gear with double-layer PMs and spoke structure for tidal power generation," *IEEE/ASME Transactions on Mechatronics*, Vol. 28, No. 6, 3263–3271, Dec. 2023.

[18] Ni, Y., X. Zhang, and L. Zhang, "Analysis of stator slot flux reverse machine with halbach array," in *2023 IEEE 6th International Electrical and Energy Conference (CIEEC)*, 4300–4303, Hefei, China, 2023.